crystals

MDPI

Article

Creep Behavior of a Single Crystal Nickel-Based Superalloy Containing High Concentrations of Re/Ru at an Intermediate Temperature

Ning Tian [1], Tai Meng [2,*], Shulei Sun [1], Shunke Zhang [1] and Danping Dang [3]

[1] Department of Mechanical and Electronic Engineering, Guizhou Communications Ployteechnic University, Guiyang 551400, China; 15185430568@163.com (N.T.)
[2] Mechanical Engineering Institute, Guizhou University of Engineering Science, Bijie 551700, China
[3] Sanmenxia Nonferrous Metals Technology Development Center, Sanmenxia 472000, China
* Correspondence: syhgxytn@163.com

Abstract: The deformation and damage mechanisms of a single crystal nickel-based superalloy containing 6.0%Re/5.0%Ru were studied through creep performance tests at 800 °C/860–880 MPa, microstructure and morphology observation, and dislocation configuration analyzation. It was found that, during the creep process at the intermediate temperature, the γ′ phase does not form a raft-like structure. After a creep fracture, the distortion degree of the cubic γ′ phase becomes greater when the observation region is closer to the fracture. The alloy has a long creep life at 800 °C, and the dislocation slipping or climbing in the γ matrix is the deformation mechanism at the early and middle creep stages. At the later creep stage, the γ′ phase is sheared by dislocations. Because of the low stacking-fault energy of the alloy, the <110> superdislocation shearing into the γ′ phase can decompose on the {111} plane to form a (1/3) <112> partial dislocation and stacking-fault configuration or cross-slip to the {100} plane to form the Kear–Wilsdorf (K-W) lock, which greatly improves the creep resistance of the alloy. At the later creep stage, the primary/secondary slip systems in the alloy are activated alternately, resulting in micro-cracks at the intersection of the two slip systems. As the creep progresses, the initiated cracks spread and propagate in the γ matrix phase along a direction normal to the stress axis and connect with each other until creep fracture occurs. This is the fracture mechanism of the alloy during creep at the medium temperature.

Keywords: Re/Ru elements; single crystal alloy; creep behavior; K-W lock; crack

Citation: Tian, N.; Meng, T.; Sun, S.; Zhang, S.; Dang, D. Creep Behavior of a Single Crystal Nickel-Based Superalloy Containing High Concentrations of Re/Ru at an Intermediate Temperature. *Crystals* **2024**, *14*, 983. https://doi.org/10.3390/cryst14110983

Received: 21 October 2024
Revised: 7 November 2024
Accepted: 12 November 2024
Published: 14 November 2024

1. Introduction

Nickel-based single-crystal superalloys have excellent high-temperature mechanical properties and are the preferred structural materials widely used in aero-engine turbine blades, which operate in high-temperature and high-stress environments [1–3]. Since creep deformation mainly occurs through dislocation movement in the γ matrix, the high-temperature creep properties of the alloys can be improved by adding refractory elements which are mainly enriched in the γ matrix. The addition of refractory elements has different effects on the phase structure, γ′/γ two-phase mismatch, element diffusion rate, defect structure, and deformation and damage mechanisms of the alloys. Therefore, the addition of refractory elements has a great influence on the mechanical properties of the alloys [4–6]. In particular, the addition of high concentrations of Re/Ru elements can greatly improve the mechanical properties [7]. Single crystal nickel-based alloys containing high concentrations of Re/Ru elements have been widely investigated by domestic and foreign studies [8–10].

There are two main deformation mechanisms during the deformation of nickel-based superalloys. Dislocations move in the softer γ matrix channel at the initial and intermediate creep stages and dislocations shear the γ′ reinforced phase at the later creep stage. Different dislocation configurations, such as intrinsic stacking faults (SISF), inverse domain

boundaries (APB), and complex stacking faults (SCF), can be generated when dislocations enter the γ' phase [11,12]. The addition of Re and Ru elements can reduce the stacking-fault energy of two γ'/γ phases in the alloys, so that the alloys in the high-temperature creep processes can more easily form stacking faults. These stacking faults are more stable, are not easy to decompose, and can impede the dislocation movement, thereby improving the mechanical properties of the alloys [13]. It was found that a single crystal alloy containing 4.5%Re and one containing 4.5%Re/3Ru had lower stacking-fault energy compared to alloys without Re and Ru [14,15]. When more and more refractory elements such as Re, Ru, and W are dissolved in the γ matrix phase, the gap between the lattice constants of the two γ'/γ phases increases, resulting in an increase in the lattice mismatch and a higher mismatch stress in the alloys. In the process of high-temperature creep, a larger mismatch stress can form dense and stable dislocation networks, which can make dislocations climb over the γ' phase and delay the shearing of dislocations into the γ' phase, resulting in an increase in the creep resistance of the alloys [16,17]. However, it is still unclear whether the stacking-fault energy of the alloys decreases with the further increase in the Re/Ru content, especially the creep behavior and deformation mechanism of a single crystal nickel-based alloy containing 6%Re/5%Ru at medium temperatures.

The refractory elements Re, Ru, and W are concentrated in the γ matrix phase [18,19]; they can enhance the strength of the γ matrix phase, but the creep damage of the γ matrix is still the main failure mode of the alloys. Therefore, the creep behavior of single crystal nickel-based alloys have been extensively studied [20,21]. At the late high-temperature creep stage, a large number of dislocations shear into the γ' phase, which loses its creep resistance, and under the action of the maximum shear stress, dislocations slip in double orientations, resulting in stress concentration occurring at the twisted interface of the two γ'/γ phases. Meanwhile, cracks are initiated and expand to form large cracks until creep fracture occurs. This is the fracture mechanism of single crystal alloys in service [22]. However, the damage and fracture mechanism of superalloys containing high concentrations of Re/Ru during medium-temperature creep is not clear.

During service, an aero-engine has to experience the process from medium temperature/high stress to high temperature/low stress, so the aero-engine blade components must withstand various working conditions from start-up to stability [23]. The creep behavior of superalloys with different compositions are different in different temperature ranges. Although there is much literature on the effects of elements on the creep behavior of superalloys, they generally only focus on the effects of single elements (Re, Ru, and W) on the creep behavior [24]. However, the effects of the interaction between Re/Ru and other elements on the microstructure evolution and creep behavior of the alloys are rarely of concern in the literature.

Therefore, in order to study the influence mechanisms of Re/Ru on the creep behavior and deformation mechanisms of superalloys, a superalloy containing 6Re%5%Ru was prepared to test its mechanical properties under medium-temperature and medium-stress conditions, and the microstructure of the alloy was observed and the dislocation configuration was analyzed.

2. Experimental Procedure

In this study, a nickel-based single crystal alloy containing high concentrations of Re/Ru with the composition of NiBal-5.5%Al-7.8%Ta-1.9%Cr-7.1%Co-3%Mo-4.8%W-6.0%Re-5.0%Ru was prepared, and the alloy specimen rods were orientated with a [001] orientation (16 mm in diameter and 150 mm in length). Due to the high content of refractory elements, the as-cast alloy was subjected to solution temperature treatment at a high-temperature interval, and the selected heat treatment regime is shown in Table 1.

Table 1. Heat treatment regimes of the alloys.

Process	Process Parameters
Solution	1300 °C × 2 h + 1310 °C × 6 h + 1315 °C × 10 h + 1323 °C × 10 h + 1328 °C × 10 h + 1332 °C × 5 h
First aging	1150 °C × 4 h, A.C.
Second aging	870 °C × 24 h, A.C.

After completing the heat treatment, the alloy test bars were prepared by wire-cutting them into specimens with cross-sections of 4.5 mm × 2.5 mm. The creep properties of the I-shaped creep specimens were tested using a GTW504 creep tester under the stress conditions of 860–880 MPa at 800 °C. The creep specimens after different creep times were air-cooled, respectively. These specimens were corroded in a corrosive solution of 5 mL H_2SO_4 + 80 mL H_2O + 20 g $CuSO_4$ + 100 mL HCl, and the microstructure was observed with a scanning electron microscope (SEM). Thin foils for transmission electron microscopy (TEM) observation were prepared by electrochemical methods from 50 to 60 μm sliced specimens in an ethanol solution of 8% perchloric acid at −30 °C and 30 mA. In order to observe the dislocation density, TEM images of samples with different creep times were processed. Firstly, a field of view with an area (S) in a TEM image was selected. The length (L) of all dislocation lines in the selected field of view was measured using image processing software to obtain the total length of dislocation lines in the field of view. The measured data were substituted into the formula $\delta = L/S$ to obtain the dislocation density (δ). In order to reduce the error, the dislocation density in each TEM image was at least the average value of the dislocation density in three fields of view.

3. Experimental Results and Analysis

3.1. The Microstructure and Creep Properties of the Alloy

The TEM microstructure morphology of the (001) crystal plane of the alloy after the heat treatment is shown in Figure 1. It shows that the alloy is composed of two γ'/γ phases. The size of the two γ'/γ phases are about 400–450 nm and 60–80 nm. The cubic γ' phase is regularly arranged along the [100] and [010] directions, as shown with the arrows. And, there are no dislocations in the observed range.

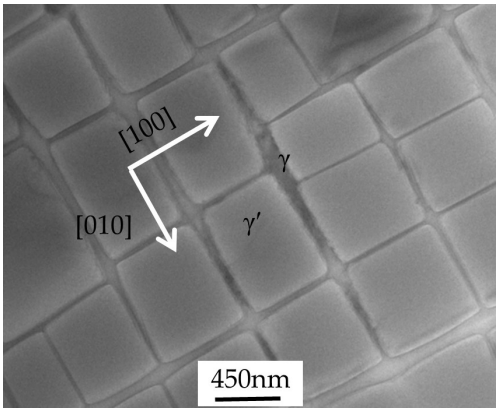

Figure 1. Microstructure of the alloy after full heat treatment.

The creep curves of the alloy were tested under the stress conditions of 860–880 MPa at 800 °C, as shown in Figure 2. It shows that the creep can be divided into initial, steady, and accelerated stages. The strain rate is larger in the initial and accelerated stages and smaller in the steady stage. The curves 1 and 2 in the figure are the creep curves of the alloy, measured at 860 MPa and 880 MPa, respectively. The strain rates during the medium-term steady state are 0.0069%/h and 0.0148%/h, and the creep life of the alloy is 286 h and 204 h, respectively.

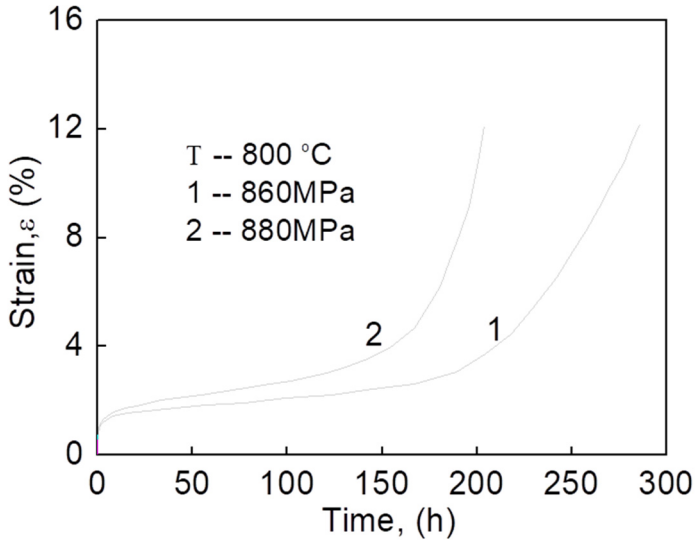

Figure 2. Creep curves of the alloy.

3.2. Microstructure Evolution During Creep

The SEM microstructure of the alloy in different regions after creep fracture at 800 °C/860 MPa is shown in Figure 3. Figure 3a is a schematic diagram of the sample observation area after the creep fracture. Figure 3b–e show the microstructures of different regions of the sample, where the dark contrast region and the light contrast region are the γ' phase and γ matrix, respectively. Thereinto, the normal orientation of the observation surface is in the [100] direction.

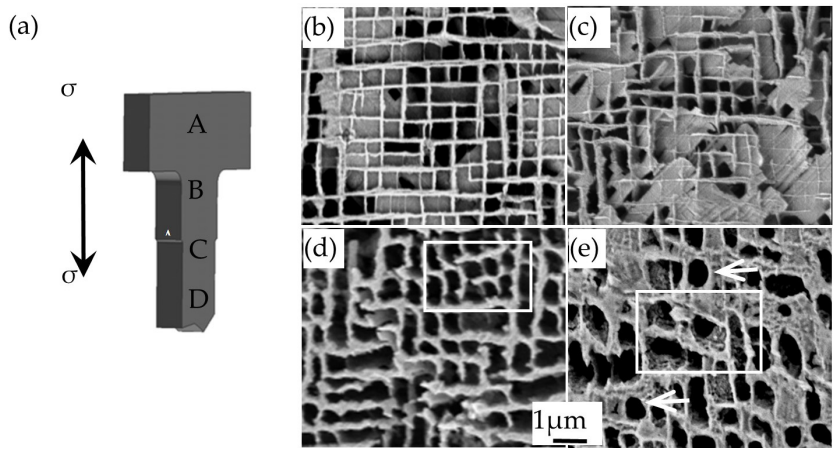

Figure 3. Microstructure in different regions of the alloy. (**a**) Schematic diagram of the observation regions in the specimen, (**b**–**e**) SEM morphologies corresponding to regions A–D of the specimen, respectively.

The morphology of the region A marked in Figure 3a is shown in Figure 3b. It shows that there is no noticeable change for the γ'/γ phases compared with the uncreeped alloy, which is due to the fact that the area is not affected by stress and the diffusion of elements at lower temperatures is small. Due to the small strain, the γ' phase in region B has only a small degree of coarsening and distortion and still maintains a good cubic degree, as shown in Figure 3c. The γ'/γ morphology of region C is shown in Figure 3d. Due to the tensile stress in this region, although the γ' phase still maintains a cubic structure, the size increases slightly, and some of the γ' phase shows distortion and corner passivation due to large plastic deformation, as shown in the white box. The γ'/γ morphology of region D is shown in Figure 3e, which is the closest to the fracture and where necking occurs, and the plastic deformation is large, resulting in increased γ'/γ distortion and coarsening. As

shown in the white box in Figure 3e, the sizes of the γ' phase and γ matrix are about 780 and 170 nm, respectively. This shows that the size and distortion of the cubic γ' phase decrease with an increasing distance from the fracture during creep at 800 °C, but the rafted structure of the cubic γ' phase is not detected.

The microstructure of the alloy during creep at 800 °C/860 MPa for different times is shown in Figure 4. The microstructure of the alloy during the steady state after creep for 60 h is shown in Figure 4a; the direction of the applied stress is shown by the double arrows in Figure 4a. The dislocation density in the alloy is calculated to be 1.1×10^{10} cm^2. It can be seen that the γ' phase still maintains a cubic shape, and no dislocations obviously shear into the γ' phase. Dislocations move in the γ matrix, which is due to the softness of the γ matrix compared to the γ' phase. And, most of the dislocations in the γ matrix move along mutually perpendicular directions which are at 45° angles relative to the stress axis, as shown with the long arrows in Figure 4a. This is due to the maximum shear stress on the dislocations in the γ matrix in this direction. Many stacking faults are found in the horizontal γ matrix, as shown in the figure. The analysis shows that Re and Ru elements distributed in the γ matrix can significantly reduce the alloy stacking-fault energy. The lower stacking-fault energy causing the dislocation to decompose is the main deformation mechanism besides the dislocation motion [13]. The stacking-fault structure is relatively stable, and a large amount of energy is needed to rebundle the stacking faults into one single dislocation. Therefore, the alloy has a longer steady-state creep time and a smaller steady-state strain rate.

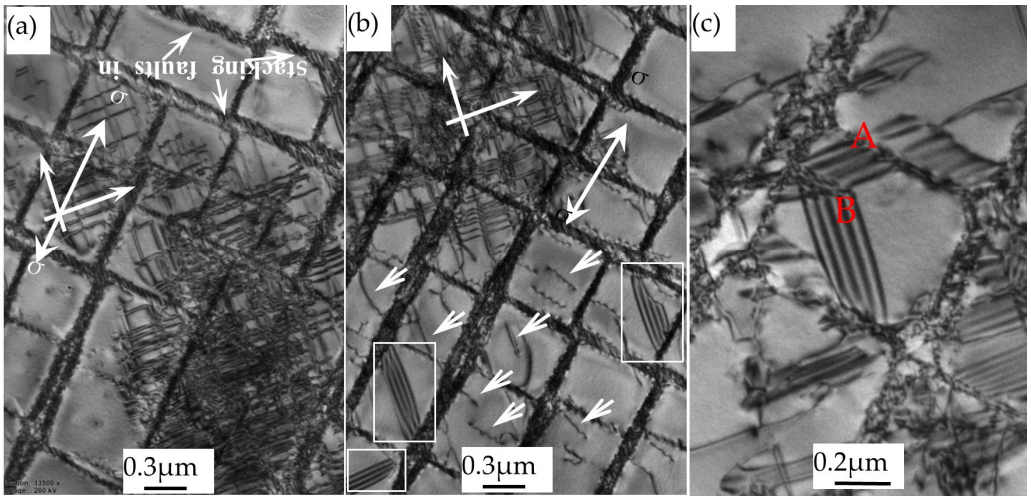

Figure 4. Morphologies of the alloy after creep tests for different times under the applied stress of 860 MPa at 800 °C. (**a**) Crept for 60 h, (**b**) crept for 286 h up to fracture, and (**c**) two stacking faults with different expansion directions.

Under this condition, the microstructure of the alloy after creep fracture is shown in Figure 4b. The dislocation in the γ matrix channel still has a double orientation slip at the 45° angle relative to the stress axis, as shown by the long arrow in Figure 4b. The dislocation density in the alloy is calculated to be 1.4×10^{11} cm^2. More dislocations can be observed in the γ' phase, as marked by the short arrows in the figure. This is related to the fact that with the progress of the creep to the later stage, a large number of deformation dislocations move to the γ/γ' interface and react with the interface dislocations generated by the mismatch stress to form dislocation tangles. Dislocation tangles tend to cause stress concentration, resulting in the damage of the γ/γ' two-phase interfacial dislocation network, which can cause deformation dislocations to shear into the γ' phase [25]. Stacking faults can be observed in the γ' phase, as shown in the box in the figure. The analysis shows that the interfacial dislocations moving to the γ/γ' two-phase interfaces can be decomposed on the {111} plane to form a/3<112> leading partial dislocations and a/6<112>

partial dislocations. The a/3<112> leading partial dislocations continue to shear into the γ' phase and the a/6<112> partial dislocations stay at the γ/γ' two-phase interfaces to form two partial dislocations plus stacking-fault configurations. Under this condition, the a/3<112> leading partial dislocations on different {111} slip planes are found in the same γ' phase in another region after the creep fracture, as marked with the letters A and B in Figure 4c, indicating that the stacking-fault energy of the alloy is low, and the dislocations shearing into the γ' phase can slip on different {111} planes.

3.3. Dislocation Configuration Analysis During Creep

The dislocation configuration in the γ' phase of the alloy after a creep rupture at 800 °C/860 MPa is shown in Figure 5. It shows that the dislocation K is the leading dislocation that shears into the γ' phase, the dislocation J is the drag dislocation at the γ/γ' two-phase interface, and the distance between the dislocations K and J is the stacking-fault propagation width. When the diffraction vector is g = [020], the partial dislocations K and J do not show contrast, as shown in Figure 5c. When the diffraction vectors are g = [11 $\bar{3}$] and g = [3 $\bar{1}$1], the partial dislocation K disappears and appears, as shown in Figures 5a and 5b, respectively. According to the invisibility criteria of g·b = 0 and g·b = ±(2/3) for dislocations, it can be confirmed that the dislocation K is a super-partial dislocation with the Burgers vector b_K = (1/3)[11 $\bar{2}$]. When the diffraction vectors are g = [11 $\bar{3}$] and g = [3 $\bar{1}$1], the dislocation J shows and does not show contrast, respectively, as shown in Figure 5a,b. According to the invisibility criteria, as above, it can be confirmed that the dislocation J is a super-partial dislocation with the Burgers vector b_J = (1/6)[1 $\bar{2}$1]. Therefore, it can be confirmed that the <110> dislocation shears into the γ' phase and decomposes, forming a dislocation configuration of two super-Shockley partial dislocations + stacking faults (SISF). According to $b_J \times b_K$ = (1 $\bar{1}$1), it can be determined that the dislocation decomposes on the (1 $\bar{1}$1) crystal plane, and the reaction formula is the following.

$$(a/2)[110]\ (1/6)[1\ \bar{2}1]_J + (\mathrm{SISF})_{(1\ \bar{1}1)} + (1/3)\ [11\ \bar{2}]_K \quad (1)$$

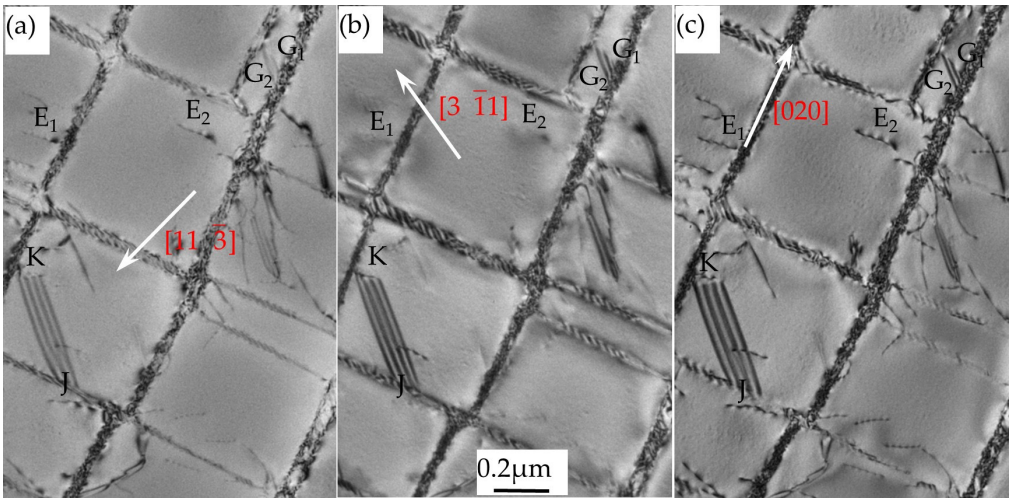

Figure 5. Dislocation configuration within the γ' phase of the alloy after being crept up to fracture at 800 °C/860 MPa. (**a**) g = [11 $\bar{3}$], (**b**) g = [$\bar{3}$ 11], (**c**) g = [020].

The superdislocations that shear into the γ' phase are marked with the letters E_1, E_2, G_1, and G_2 in Figure 5. When the diffraction vectors are g = [11 $\bar{3}$] and g = [020], E_1 and E_2 display contrast, as shown in Figure 5a,c. When the diffraction vector is g = [3 $\bar{1}$1], E_1 and E_2 do not display contrast, as shown in Figure 5b. According to the invisibility criterion of dislocation contrast, it is determined that the dislocations E_1 and E_2 are superdislocations with the Burgers vector of b = [011]. In addition, because the dislocations E_1 and E_2 have the same direction, the line vector is μ = [0 $\bar{2}$2], so the slip surface of the dislocations can be

identified as $b'\mu$ = (100). When the diffraction vector is g = [11 $\bar{3}$], G_1 and G_2 do not show contrast, as shown in Figure 5a. When the diffraction vectors are g = [3 $\bar{1}$1] and g = [020], G_1 and G_2 show contrast, as shown in Figure 5b,c. According to the invisibility criterion of dislocation contrast, the possible Burgers vectors of dislocations G_1 and G_2 are determined to be superdislocations with b = [1 $\bar{1}$0]. Because the line vectors of the dislocations G_1 and G_2 are μ = [220], the slip surface of the dislocation G can be identified as $b \times \mu$ = (001).

It can be observed that the dislocations activated during creep first slip in the {111} planes of the γ matrix. As the creep enters the later stage, the dislocations shear into the γ' phase and can slip from the {111} plane to the {100} plane under the action of the applied stress to form a Kear–Wilsdorf lock. Since the activation of the Kear–Wilsdorf dislocation lock requires high energy, the Kear–Wilsdorf lock can effectively improve the mechanical properties of the alloy. In addition, the dislocation G can cross-slip to the {100} plane and can be decomposed to form a dislocation configuration of two partial dislocations + anti-phase boundary (APB). The reaction formula is the following.

$$a[110]_G = (a/2)[1\,\bar{1}0]_{G1} + \mathrm{APB}_{(100)} + (a/2)[1\,\bar{1}0]_{G2} \quad (2)$$

3.4. Damage and Fracture During Creep

The morphology of crack initiation and propagation in the near fracture area of the alloy after creep at 800 °C/860 MPa for different times is shown in Figure 6. The direction of the applied stress is shown by the double arrows in Figure 6a,c. Figure 6a shows the microstructure of the alloy after 200 h of creep. It can be seen that the two γ'/γ phases are twisted at a fixed angle, as shown by the short white arrow in the figure. According to analysis, this is due to the start of the main slip trace line with a width of about 150 nm at a 45° angle relative to the stress axis, which leads to opposite stress on both sides of the slip band, as indicated in Figure 6a. As the creep proceeds, the secondary slip system starts, and as the primary/secondary slip system alternately start, microcracks are generated at the γ/γ' two-phase interface at the intersection of the two slip systems, as shown in region H of Figure 6b.

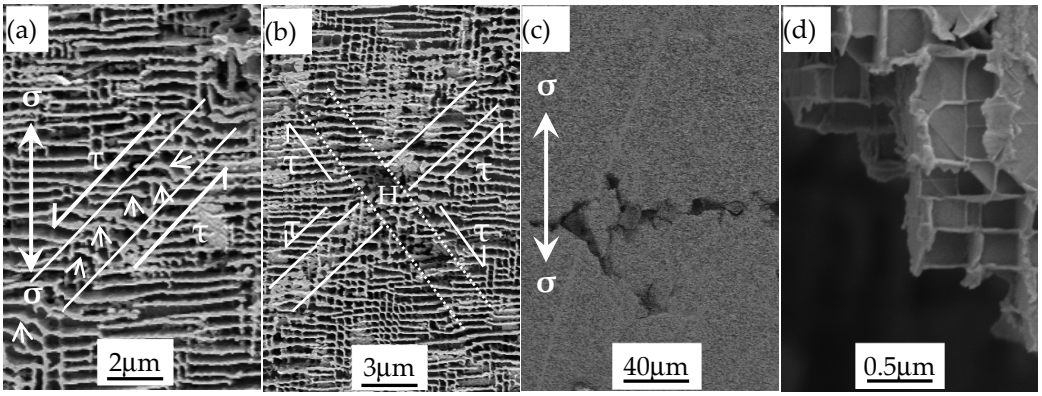

Figure 6. The crack initiation and propagation morphology in the alloy after creep for different times. (**a**) Crept for 200 h, (**b**) crept for 240 h, (**c**) crept for 286 h up to fracture, and (**d**) the local amplification of the creep fracture.

With the progress of creep, cracks continuously initiate and expand to form large cracks, which can make the creep fracture of the alloy rapid. The direction of the crack extension is perpendicular to the stress axis, as shown in Figure 6c. The local amplification diagram of the crack is shown in Figure 6d. It can be seen that the γ' phase boundary of the alloy after the creep fracture is clear and maintains a complete cubic state with no cracks cutting in, indicating that the crack is initiated and propagated along the γ/γ' two-phase interfaces. The reason for this is that a large amount of Re/Ru is added to the alloy and mainly enriched in the γ matrix phase, while the γ matrix phase is still the weak link of the alloy. Most of the dislocations are generated in the γ matrix and move in the γ matrix,

where they become entangled and are susceptible to stress concentration. As the creep proceeds, the stress concentration degree grows, and when it reaches the combined strength critical value, cracks initiate in the γ matrix. Therefore, the fracture mechanism of the alloy is that the primary/secondary slip systems start alternately in turn, and microcracks are generated at the γ/γ′ two-phase interfaces at the intersection of the primary/secondary slip systems. And, the initiated cracks propagate and expand in the γ matrix phase along a direction perpendicular to the stress axis and connect with each other, which makes the creep fracture of the alloy rapid.

4. Discussions

4.1. Influencing Factors of Dislocation Decomposition in γ′ Phase

The dislocations that shear into the γ′ phase can decompose under the applied stress to form different types of stacking faults. Studies have shown that there are three types of stacking faults in the γ′ phase with a face-centered cubic structure, namely intrinsic stacking faults (SISF), an inverse phase boundary (APB), and complex stacking faults (SCF) [26].

For this alloy, during creep at 1170 °C/110 MPa, only a small amount of an antiphase domain boundary (APB) is found in the γ′ phase [22], and the dislocations that shear into the γ′ phase during the acceleration creep stage at 800 °C/860 MPa can be decomposed to form two types of stacking faults, SISF and an APB, as shown in Figures 4 and 5. It can be observed that this is caused by two reasons. (1) The addition of high concentrations of Re and Ru reduces the stacking-fault energy of the alloy, so the alloy in the creep process can form a variety of faults, and in the intermediate-temperature creep process, these different types of dislocations can be preserved, but in the ultra-high-temperature creep process, thermal activation can make the faults rebundle into one single dislocation. (2) During the creep process and with an increase in temperature, the free energy of the stacking faults increases, which results in an increase in the alloy's stacking-fault energy and causes a small number of stacking faults in the alloy during high-temperature creep.

The mechanism of dislocation decomposition, producing different stacking faults, is shown in Figure 7. Thereinto, the black dots denote Al atoms, the white dots are Ni atoms, Re and W are represented by the blue dots, and Ru atoms are represented by the red dots. Ru in the γ′ phase mainly occupies the position of the face-centered cubic vertex, and Ru has strong adsorption properties, which allows heavy metal elements to attach to the vicinity of Ru atoms. Ru can hybridize with adsorbed atoms (Re and W), as indicated by the darker areas in the figure, and the darker colors indicate stronger bonding. The dots in the figure are divided into three types, those with large, medium, and small radii, which, respectively, represent the projection of the three-layer crystal plane atoms adjacent to the {111} plane on the (111) plane.

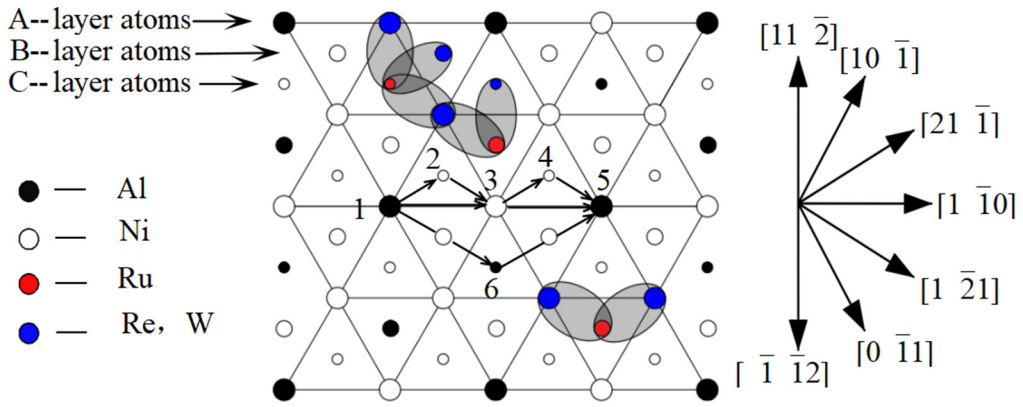

Figure 7. Schematic diagram of dislocations decomposing into different plane defects in $L1_2$-Ni_3Al.

During creep, when the leading dislocation formed by dislocation decomposition moves along the 1→6→5 path, as in Figure 7, the intrinsic stacking fault (SISF) can be left

at site 6 in the crystal, and the (1/3)<112> and (1/6)<112> partial dislocations can be left at sites 1 and 5, respectively. When the dislocation moves along the 1→3→5 direction, the (a/2)<110> partial dislocations can be left at sites 1 and 5, respectively, and the antiphase boundary (APB) can be formed at site 3 in the crystal. The complex stacking fault (SCF) can be produced at site 2 when the dislocation moves along the 1→2→3 path. It is found that the formation energies of the SISF, APB, and CSF in the {111} plane of Ni-based single crystal alloys increase successively, and the formation energy of the APB in the {100} plane is smaller than that of the SISF in the {111} plane [27]. In this alloy, no surface defects with CSF characteristics were observed during creep at 800 °C. Only SISF on the {111} plane and partial dislocations sliding to the {100} plane plus APB dislocation structures were observed, as shown in Figures 4 and 5. This is the same as the previous research results. It can be seen that there are many types of stacking faults in the alloy, and it can be considered that the addition of Ru in the alloy greatly increases the hybridization of Ru, Re, and W atoms, resulting in a uniform decrease in the generalized stacking-fault energy (the SISF, APB, and CSF formation energy in the {111} and {100} planes) of the alloy.

4.2. Theoretical Analysis of Crack Initiation and Propagation

Crack initiation and propagation occur at the later stage. This is due to the fact that the γ/γ' two-phase dislocation network is destroyed at the later stage of creep, and the dislocations shear into the γ' phase along the damage which slips under the maximum shear stress with a 45° angle relative to the stress axis, resulting in the starting of the main slip system. As the creep progresses, the deformation becomes larger and larger. To release the stress caused by the deformation, the secondary slip system is then activated. Due to the alternating activation of the primary/secondary slip systems, a large degree of plastic deformation occurs at the intersection of the two slip systems, and microcracks are generated there. As the creep continues, the microcracks are subjected to increasing transverse stress to make them expand, resulting in the rapid instability and fracture of the alloy.

A schematic diagram of crack initiation and propagation is shown in Figure 8. At the later stage of creep, dislocations shear into the γ' phase along the damaged dislocation network and begin to slip under the action of the maximum shear stress (τ), resulting in the start of the main slip system. Due to the opposite direction of the shear stress (τ) on both sides of the slip band, the rafted γ' phase in the alloy is distorted along the direction of the main slip system, as shown in Figure 8a. As the creep proceeds, the secondary slip system starts in another orientation, causing the γ' phase to twist again, as shown in Figure 8b. A large degree of plastic deformation occurs at the intersection of the two slip systems, and microcracks are generated, as shown in the black area in Figure 8b. The analysis shows that there are high concentrations of Re and Ru in the γ matrix of the alloy. These Re and Ru elements have strong binding forces. When the dislocations move to the vicinity of the Re and Ru clusters, they are "rebounded" back to the γ phase and continue to slip. After the dislocations encounter the Re and Ru clusters again, the "rebounding" occurs again, so the crack only initiates and expands in the γ matrix.

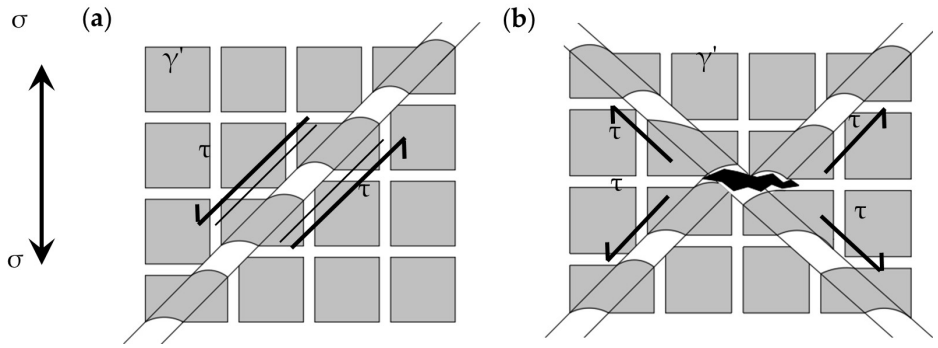

Figure 8. Schematic diagram of crack initiation and propagation. (**a**) crack initiation (**b**) crack propagation.

With the progress of creep, the neck-shrink of the alloy increases gradually, and the primary and secondary slip systems are repeatedly activated, which further increases the distortion degree of the γ' phase. Under the action of transverse stress, the crack expands in a direction perpendicular to the stress axis, and the small cracks gradually expand into large cracks. As the creep proceeds, the large cracks are connected to each other, the alloy's effective area under the force decreases rapidly, the strain rate increases rapidly, and the alloy breaks quickly.

5. Conclusions

(1) During the process of medium-temperature creep, the alloy containing 6.0%Re/5.0%Ru has good creep resistance and long creep life, the γ' phase does not form a rafted structure, and a large number of stacking faults are formed in the γ and γ' phases, indicating that the alloy has a lower stacking-fault energy. The lower stacking-fault energy can make dislocations form more stacking faults, which can reduce the steady-state creep rate and enhance the creep resistance of the alloy.

(2) The deformation mechanism of the alloy during creep is dislocations slipping in the matrix and shearing into the γ' phase. The superdislocations that shear into the γ' phase can decompose on the {111} plane to form the dislocation configuration of (1/3) partial dislocation plus stacking faults and can also cross-slip from the {111} plane to the {100} plane to form a K-W locking form of (1/2) <110> +APB. Both dislocation configurations can inhibit the dislocation movement to improve the creep resistance of the alloy.

(3) The fracture mechanism during medium-temperature creep is that the main/secondary slip systems of the alloy are activated alternately and microcracks are generated at the γ/γ' two-phase interfaces at the intersection of the main/secondary slip systems. The initiated cracks propagate and expand in the γ matrix phase along a direction perpendicular to the stress axis and are connected with each other to result in creep fracture.

Author Contributions: Conceptualization, N.T.; methodology, T.M.; software, S.S. and S.Z.; data curation, D.D. All authors have read and agreed to the published version of the manuscript.

Funding: The sponsorship of this research from the Guizhou Province Science and Technology Plan Project (QKHJC-ZK[2024] yiban604), Sanmenxia City Science and Technology Bureau Science and Technology Research Project (2022002005), Intelligent Transportation Equipment Manufacturing Technology Innovation Team Project (qianjiaoji [2023]100), and Natural science research project of the Education Department of Guizhou Province (qianjiaoji[2023]1100) are gratefully acknowledged, and Guizhou Sci-Tech Cooperation Platform Talent-CXTD[2021]008.

Data Availability Statement: The original contributions presented in the study are included in the article, further inquiries can be directed to the corresponding author/s.

Conflicts of Interest: The authors declare no conflict of interest.

References

1. Tang, Y.T.; D'Souza, N.; Roebuck, B.; Karamched, P.; Panwisawas, C.; Collins, D.M. Ultra-high temperature deformation in a single crystal superalloy: Mesoscale process simulation and micromechanisms. *Acta Mater.* **2021**, *203*, 116468. [CrossRef]
2. Tian, S.-G.; Liang, F.-S.; Li, A.-N.; Li, J.-J.; Qian, B.-J. Microstructure evolution and deformation features of single crystal nickel-based superalloy containing 4.2% Re during creep. *Trans. Nonferrous Met. Soc. China* **2011**, *21*, 1532–1537. [CrossRef]
3. Tian, N.; Tian, S.; Yan, H.; Shu, D.; Zhang, S.; Zhao, G. Deformation mechanisms and analysis of a single crystal nickel-based superalloy during tensile at room temperature. *Mater. Sci. Eng. A* **2019**, *744*, 154–162. [CrossRef]
4. Van Sluytman, J.S.; Pollock, T.M. Optimal precipitate shapes in nickel-base γ-γ' alloys. *Acta Mater* **2012**, *60*, 1771–1783. [CrossRef]
5. Zhang, Y.; Liu, L.; Huang, T. Initial melting and solution treatment of a third-generation nickel-based single crystal superalloy containing boron. *Rare Met. Mater. Eng.* **2017**, *46*, 3105–3110.
6. Lv, X.; Zhang, J. Three-dimensional geometry of "square-like" dislocation network in nickel-base single crystal superalloy. *J. Alloy. Compd.* **2016**, *688*, 449–455. [CrossRef]
7. Heckl, A.; Neumeier, S.; Göken, M.; Singer, R.F. The effect of Re and Ru on γ/γ' microstructure, γ-solid solution strengthening and creep strength in nickel-base superalloys. *Mater. Sci. Eng. A* **2011**, *528*, 3435–3444. [CrossRef]

8. Zhao, P.; Xie, G.; Chen, C.J.; Wang, X.L.; Zeng, P.L.; Wang, F.; Zhang, J.; Du, K. Interplay of Chemistry and Deformation-Induced Defects on Facilitating Topologically-Close-Packed Phase Precipitation in Nickel-Base Superalloys. *Acta Mater.* **2022**, *236*, 118109. [CrossRef]
9. Heckl, A.; Neumeier, S.; Cenanovic, S.; Göken, M.; Singer, R. Reasons for the enhanced phase stability of Ru-containing nickel-based superalloys. *Acta Mater.* **2011**, *59*, 6563–6573. [CrossRef]
10. Wang, X.G.; Liu, J.L.; Jin, T.; Sun, X.; Hu, Z.; Do, J.; Choi, B.; Kim, I.; Jo, C. Dislocation motion during high-temperature low-stress creep in Ru-free and Ru-containing single-crystal superalloys. *Mater. Des.* **2015**, *67*, 543–551. [CrossRef]
11. Asadi, E.; Zaeem, M.A.; Moitra, A.; Tschopp, A.M. Effect of vacancy defects on generalized stacking fault energy of fcc metals. *J. Phys. Condens. Matter* **2014**, *26*, 115404. [CrossRef]
12. Long, H.B.; Wei, H.; Liu, Y.N.; Mao, S.C.; Zhang, J.X.; Xiang, S.S.; Chen, Y.H.; Gui, W.M.; Li, Q.; Zhang, Z.; et al. Effect of lattice misfit on the evolution of the dislocation Structure in Ni-based single crystal superalloys during thermal exposure. *Acta Mater.* **2016**, *120*, 95–107. [CrossRef]
13. Bachurin, D.V.; Weygand, D.; Gumbsch, P. Dislocation-grain boundary interaction in <111> textured thin metal films. *Acta Mater.* **2010**, *58*, 5232–5241. [CrossRef]
14. Ma, S.; Carroll, L.; Pollock, T.M. Development of phase stacking faults during high temperature creep of Ru-containing single crystal superalloys. *Acta Mater.* **2007**, *55*, 5802–5812. [CrossRef]
15. Wang, X.G.; Liu, J.L.; Jin, T.; Sun, X.F. The effects of ruthenium additions on tensile deformation mechanisms of single crystal superalloys at different temperatures. *Mater. Des.* **2014**, *63*, 286–293. [CrossRef]
16. Carroll, L.J.; Feng, Q.; Pollock, T.M. Interfacial Dislocation Networks and Creep in Directional Coarsened Ru-Containing Nickel-Base Single-Crystal Superalloys. *Metall. Mater. Trans. A* **2008**, *39*, 1290–1307. [CrossRef]
17. Huang, S.; Huang, M.; Li, Z. Effect of interfacial dislocation networks on the evolution of matrix dislocations in nickel-based superalloy. *Int. J. Plast.* **2018**, *110*, 1–18. [CrossRef]
18. Shu, D.; Tian, S.; Tian, N.; Liu, L.; Liang, S.; Zhang, B. Influence of Re/Ru on concentration distribution in the/phase of nickel-based single crystal superalloys. *Mater. Des.* **2017**, *132*, 197–207. [CrossRef]
19. Liu, C.; Yang, W.; Cao, K.; Qu, P.; Qin, J.; Zhang, J.; Liu, L. New insights into the microstructural stability based on the element segregation behavior at γ/γ interface in Ni-based single crystal superalloys with Ru addition. *J. Mater. Sci. Technol.* **2023**, *154*, 232–240. [CrossRef]
20. Tan, X.P.; Liu, J.L.; Jin, T.; Hu, Z.; Hong, H.; Choi, B.; Kim, I.; Jo, C. Effect of ruthenium on high-temperature creep rupture life of a single crystal nickel-based superalloy. *Mater. Sci. Eng. A* **2011**, *528*, 8381–8388. [CrossRef]
21. Reed, R.C.; Yeh, A.C. Identification of the partitioning characteristics of ruthenium in single crystal superalloys using atom probe tomography-ScienceDirect. *Scr. Mater.* **2004**, *51*, 327–331. [CrossRef]
22. Ning, T.; Guoqi, Z.; Tai, M.; Sugui, T.; Lirong, L.; Huajin, Y.; Guangyan, W.; Fangwei, J. Ultra-high-temperature creep behavior of a single-crystal nickel-based superalloy containing 6% Re/5% Ru. *Mater. Charact.* **2021**, *180*, 111394. [CrossRef]
23. Yan, H.; Tian, S.; Zhao, G.; Tian, N.; Zhang, S.; Liu, L. Deformation features and affecting factors of a Re/Ru-containing single crystal nickel-based superalloy during creep at elevated temperature. *Mater. Sci. Eng. A* **2019**, *768*, 138437. [CrossRef]
24. Yan, H.; Tian, S.; Zhao, G.; Tian, N.; Zhang, S. Creep and damage of a Re/Ru-containing single crystal nickel-based alloy at high temperature. *Mater. Sci. Eng. A* **2021**, *808*, 140870. [CrossRef]
25. Knowles, D.M.; Chen, Q.Z. Superlattice stacking fault formation and twinning during creep in/single crystal superalloy CMSX-4. *Mater. Sci. Eng. A* **2003**, *340*, 88–102. [CrossRef]
26. Lue, B.L.; Chen, G.Q.; Qu, S.; Su, H.; Zhou, W.L. First-principle calculation of yield stress anomaly of Ni3Al-based alloys. *Mater. Sci. Eng. A* **2013**, *565*, 317–320. [CrossRef]
27. Zhang, J.-S. *High Temperature Deformation and Fracture of Materials*; Beijing Science Press: Beijing, China, 2004; p. 23. [CrossRef]